Structure
Article

Structural Insights into the Oligomerization and Architecture of Eukaryotic Membrane Pore-Forming Toxins

Ariel E. Mechaly,[1,5,6] Augusto Bellomio,[1,2,5,7] David Gil-Cartón,[3] Koldo Morante,[1,2] Mikel Valle,[2,3] Juan Manuel González-Mañas,[1,2] and Diego M.A. Guérin[1,2,4,*]
[1]Unidad de Biofísica (CSIC-UPV/EHU)
[2]Departamento de Bioquímica y Biología Molecular, Facultad de Ciencia y Tecnología
Universidad del País Vasco, Barrio Sarriena S/N, 48940, Leioa, Vizcaya, Spain
[3]Structural Biology Unit, Cooperative Center for Research in Biosciences, 48160 Derio, Spain
[4]Fundación Biofísica Bizkaia, Campus Universitario de Leioa, Barrio Sarriena S/N, 48940 Leioa, Vizcaya, Spain
[5]These authors contributed equally to this work
[6]Present address: Unité de Biochimie Structurale, Institut Pasteur, 75724 Paris, France
[7]Present address: Departamento de Bioquímica de la Nutrición, Instituto Superior de Investigaciones Biológicas, 4000 S. M. de Tucumán, Argentina
*Correspondence: diego.guerin@ehu.es
DOI 10.1016/j.str.2010.11.013

SUMMARY

Pore-forming toxins (PFTs) are proteins that are secreted as soluble molecules and are inserted into membranes to form oligomeric transmembrane pores. In this paper, we report the crystal structure of Fragaceatoxin C (FraC), a PFT isolated from the sea anemone *Actinia fragacea*, at 1.8 Å resolution. It consists of a crown-shaped nonamer with an external diameter of about 11.0 nm and an internal diameter of approximately 5.0 nm. Cryoelectron microscopy studies of FraC in lipid bilayers reveal the pore structure that traverses the membrane. The shape and dimensions of the crystallographic oligomer are fully consistent with the membrane pore. The FraC structure provides insight into the interactions governing the assembly process and suggests the structural changes that allow for membrane insertion. We propose a nonameric pore model that spans the membrane by forming a lipid-free α-helical bundle pore.

INTRODUCTION

The integrity of the plasma membrane is crucial for the appropriate function and stability of living cells. Many pathogens induce injury to target cells through the action of diverse toxic proteins that create membrane pores. These nonselective holes breach the cell wall, producing an ion imbalance or uncontrolled ion efflux and permeabilization to a variety of molecules depending on the pore size (Iacovache et al., 2008; Tweten, 2005). Thus, the action of these pore-forming molecules disturbs the membrane integrity and can lead to cell death (Bischofberger et al., 2009).

Pore-forming toxins (PFTs) are produced by a wide range of organisms, such as bacteria, insects, marine invertebrates, poisonous reptiles, and mammals, for different purposes, including defense, attack, or signaling (Parker and Feil, 2005). In humans, it has been postulated that fibrillar amyloid deposits that result from neurodegenerative diseases can form ring-shaped structures that are very similar to bacterial PFTs (Lashuel and Lansbury, 2006), and it is known that Bcl2-like proteins trigger apoptosis by creating pores in mitochondrial membranes (Kroemer et al., 2007). Additionally, structural analysis has revealed similarities between some bacterial PFTs and other proteins that perform a range of functions (Anderluh and Lakey, 2008). Because of the above-mentioned properties for recognizing and permeabilizing biological membranes, these pores have potential medical applications in cancer therapeutics (Abrami et al., 2008; Panchal et al., 2002; Potrich et al., 2005) and biosensor technology (Astier et al., 2005).

PFTs are generally secreted as soluble monomers that diffuse toward the membrane of a target cell. Upon membrane binding, the monomers undergo a conformational change that exposes an amphipathic surface, which drives membrane insertion. The transition from the bound to inserted state usually takes place through an oligomeric intermediate commonly known as the *prepore* (Walker et al., 1992, 1995).

PFTs are usually classified according to the type of secondary structure elements they use to cross the lipid bilayer upon pore formation (Gouaux, 1997). Hence, these toxins are usually divided into two categories: α-PFTs and β-PFTs. The atomic structures of several PFTs in their water-soluble state are known (Iacovache et al., 2010), while a few structures of the oligomeric state have been solved. Prime examples include the crystal structure of the *Staphylococcus aureus* α-hemolysin pore (Song et al., 1996) and the structure of the water-soluble state of its homolog, Panton-Valentine leukocidin (Olson et al., 1999). These two structures provide insight into how β-PFTs oligomerize to eventually form a pore. Another important example is the structure of perfringolysin O in its water-soluble state (Rossjohn et al., 1997) and models of both prepore and pore forms based on EM data (Dang et al., 2005). In addition to the heptameric α-hemolysin from *S. aureus,* the crystal structure

of the dodecameric α-PFT cytolysin A (ClyA) from *Escherichia coli* has also been solved. ClyA is the only PFT for which the structures of both the soluble state (Wallace et al., 2000) and the assembled pore state (Mueller et al., 2009) have been reported.

One of the representatives of the α-PFT group is a family of eukaryotic toxins called actinoporins, or cytolysins (Alegre-Cebollada et al., 2007; Kristan et al., 2009). Actinoporins are extremely potent cytolytic toxins produced by sea anemones, endowed with both predatory and defense functions (Alvarez et al., 2009; Kristan et al., 2009). Equinatoxin-II (Eqt-II) from *Actinia equina* and sticholysin-II (Stn-II) from *Stichodactyla helianthus* are two members of this family whose three-dimensional (3D) structures have been solved by X-ray crystallography (Athanasiadis et al., 2001; Mancheno et al., 2003). They consist of a β sandwich core flanked by two short α helices. The N-terminal α helix is amphipathic and seems to be able to detach from the main body of the molecule to participate in the formation of the pore wall (Hong et al., 2002).

Crosslinking experiments (Belmonte et al., 1993), kinetic data (Tejuca et al., 1996), and electron microscopy analyses of two-dimensional (2D) crystals (Mancheño et al., 2006; Martin-Benito et al., 2000) have suggested that the pore is formed by three or four weakly interacting protomers. Each protomer contributes to the pore with its N-terminal α helix (Hong et al., 2002; Kristan et al., 2007), and three to four protomers are clearly insufficient to line a pore with a functional diameter of ~2.0 nm (Alvarez et al., 2009; Kristan et al., 2009). Therefore, the currently accepted model for actinoporin pores, the *toroidal* model, assumes that the pore consists of a toxin tetramer with lipids in the space between the protomers (Alvarez et al., 2009; Kristan et al., 2009; Mancheno et al., 2003). The participation of lipids as part of the pore wall has also been proposed for α-helical peptides such as melitin, an extract of bee venom (Allende et al., 2005; Yang et al., 2001), and for colicin E1, another α-PFT (Sobko et al., 2004). The recently reported structure of α-PFT ClyA (Mueller et al., 2009) shows 12 protomers assembled into a cylinder and supports a novel idea: a compact α-helical barrel architecture motif for α-PFT pores. Moreover, because the assembly pathway proposed for ClyA is strikingly similar to that of α-hemolysin, a common mechanism of membrane permeation that includes a nonpenetrating ring has recently been proposed for α- and β-PFTs (Bayley, 2009).

Because most α-PFTs do not form well-defined stable oligomeric complexes, the mechanisms driving oligomer association and the transition from the prepore to pore state are still unclear (Iacovache et al., 2010). These mechanisms are partly understood for β-PFTs, for which it is assumed that more than one assembly pathway may lead to completion of the ring-like pore-forming complex (Gonzalez et al., 2008).

To provide further structural information about the oligomeric nature and pore architecture of PFTs, we determined the structure of Fragaceatoxin C (FraC), an actinoporin from the sea anemone *Actinia fragacea* (Bellomio et al., 2009). Here, we present the crystal structure of a FraC nonamer and the cryoelectron microscopy (cryo-EM) reconstruction of a fully assembled FraC pore inserted in a lipid vesicle. The crystal structure displays a nonlytic nonamer, or prepore, and provides mechanistic insights into the molecular determinants governing pore assembly and detachment of the N terminus for insertion into the membrane. The cryo-EM reconstruction displays a FraC functional pore fully compatible with the crystallographic model. Our results support a pore model in which the membrane-spanning region is a compact, lipid-free α-helical bundle.

RESULTS

FraC Crystal Structure

One method for inducing oligomerization of PFTs in solution is to incubate the toxin with an appropriate detergent (Eifler et al., 2006). FraC was crystallized in the presence of the detergent N,N-dimethyldodecylamine N-oxide (LDAO) (Mechaly et al., 2009). The crystal structure of FraC was solved at 1.8 Å resolution by molecular replacement (MR) and using the atomic coordinates of Eqt-II (RCSB PDB Code 1IAZ) as search model. The MR solution contains six copies of the search model per asymmetric unit (ASU). This solution was used to build the initial FraC model and then to proceed with the refinement up to reach the final parameters indicated in Table S1 (available online). A clear electron density was observed for residues 2 to 178 in the six copies present in the ASU. The six protomers are arranged as two groups of three protomers facing each other. The ASU represents one-third of two concentric and identical crown-shaped nonamers, and the crystal packing can be described as alternatively oriented layers of hexagonal arrays of nonamers in which the central axis is parallel to the crystallographic z axis (Figures 1A and 1B). The overall external diameter of each crown is 11.2 nm, and the internal diameter is approximately 5.2 nm (Figures 1C and 1D). The interface between neighboring protomers involves a small contact area of ~600 $Å^2$ (Figures 1E and 1F) constituting a singular protomer-protomer assembly (see below). The shape complementarity of protein-protein interfaces (Lawrence and Colman, 1993) between FraC protomers is 0.66, a value comparable to those observed in antibody-antigen complexes (0.66–0.68) and in other oligomeric interfaces (Garcia et al., 1998). Between two adjacent protomers, there are various hydrogen bonds and hydrophobic contacts (Table S2).

In total, 54 LDAO detergent molecules (18 per ASU) were modeled at the interface between two stacking nonamers. These molecules are located within a region that corresponds to the basal crown rim (Figures 2A and 2B). Some of the LDAO molecules mediate contacts between protomers of the facing rings (Figure 2C), and other are contoured by aromatic residues belonging to a single protomer (Figure 2D). The detergent-rich interface between two facing rings do not involve direct protein-protein contacts but detergent-mediated interactions.

Each FraC protomer consists of a β sandwich core made of ten β strands and flanked by three helices (Figures 3A and 3B). The N terminus is attached to the β sandwich and contains a short β strand (residues 8–10), a one-turn 3_{10} helix (3_{10}, residues 11–14), and a short α helix (α_1, residues 16–24) (Figure 3B). The nine N termini line the inner FraC crown wall (Figures 1C and 1D). The interface between the N terminus and the protein core corresponds to a buried, solvent-accessible surface of about 948 $Å^2$ (Table S3 and Supplemental Experimental Procedures). Through this interface, three types of intramolecular

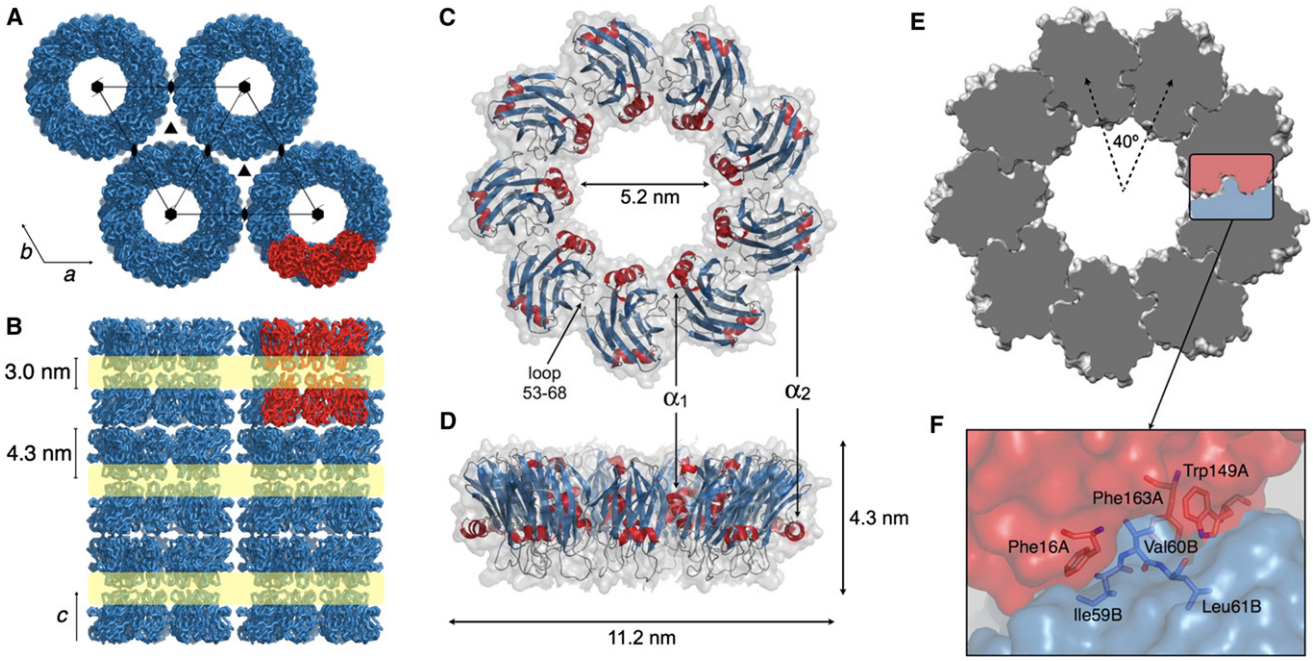

Figure 1. FraC Crystal Structure

(A) FraC crystallized in the space group $P6_322$ and six molecules (protomers) make up the crystallographic ASU. Within the ASU the protomers are arranged as two facing groups, each group consisting of three adjacent protomers (highlighted in red). The ASU constitutes of one-third of two concentric and identical ring-shaped nonamers.

(B) Applying the crystallographic symmetry, a pattern of stacked layers with opposite orientations along the z axis emerges. These layers alternatively interact through hydrophilic and detergent-rich regions (shaded in yellow) (see Figure 2).

(C) Top and (D) side views of the FraC nonamer in a ribbon representation, in which the helices are colored red and the β strands blue. The exposed loops and the molecular surface are shown in gray. In the crown-shaped FraC nonamers, the N-terminal α helices (α_1) line the inner wall of the complex and the C-terminal α helices (α_2) form an outer belt.

(E) Neighboring protomers display high shape complementarity, resembling a "mortise and tenon" joint that keeps the protomers together. The relative rotation between adjacent protomers is 40° (dashed "V").

(F) Val60 (indicated as Val60B) protrudes from one protomer (in blue) and inserts into the hydrophobic cavity lined by residues Phe16, Trp149, and Phe163 (indicated with an "A") of the adjacent protomer (in red).

interactions may contribute to maintaining the N terminus in this conformation: (1) a salt bridge formed between Asp10 and Lys69 located at the N terminus of the α_1 helix, (2) hydrophobic interactions between the side chains of residues Val8, Leu14, Leu19, Leu23, and Leu26 and the inner face of the β sandwich core, and (3) a hydrogen-bond at the C terminus of the α_1 helix between Lys32 and Gly27 (Figure 3C).

The protomer C terminus includes an α helix (α_2, residues 130–138) attached to the β sandwich core at the opposite side to which is located the N terminus (Figure 3B). In the nonamer, the α_2 helices form a belt around the outer face (Figures 1C and 1D). The α_2 helix axis is oriented nearly perpendicular to the neighboring β strands. Within this helix, residues Tyr133, Tyr137, and Tyr138 have their aromatic side chain pointing toward the LDAO molecules (Figure 2D). This region of FraC contains a chain segment rich in aromatic amino acids that includes residues Tyr108, Tyr110, Trp112, Tyr113 (Figure 3E). We will refer to this part of the FraC structure as the *basal* region. In the oligomer structure this region constitutes part of the crown base and most of the aromatic residues within this region have their side chains in contact with detergent molecules (Figure 2). Both regions, the α_2 helix and the aromatic-rich loop, contain many highly conserved residues, and in Stn-II form the phosphocholine (POC) binding site that appears to participate in phospholipid recognition (Mancheno et al., 2003) (Figure S1). In particular, residues Trp112 and Tyr113 seem to play a crucial role in sphingomyelin (SM) binding (Bakrac et al., 2008). In FraC structure this binding site encompasses the side chains of residues Ser54, Val87, Ser105, Pro107, Tyr113, Tyr133, Tyr137, and Tyr138 (Figure 3E).

The assembly between protomers involves the long loop between strands β_3 and β_4 of one monomer (residues 53–68) (Figure 3A), which is embedded into a grove at the neighboring protomer formed by the α_1 helix and the β sandwich core (Figures 1E and 1F). At the protomer interface, Val60 protrudes from one of the protomers and penetrates a cavity that harbors the Phe16-Trp149-Phe163 aromatic cluster in the next subunit (Figure 1F). This hydrophobic assembly looks like a "mortise and tenon" joint that is comprised of two components: the mortise hole (female) in one protomer and the tenon (male) that protrudes from the neighboring protomer (Figure 1E).

Comparison with Other Actinoporins

The FraC protomer fold is identical to the fold of the other known actinoporins solved in a water-soluble state. This was not unexpected because a high degree of sequence identity and

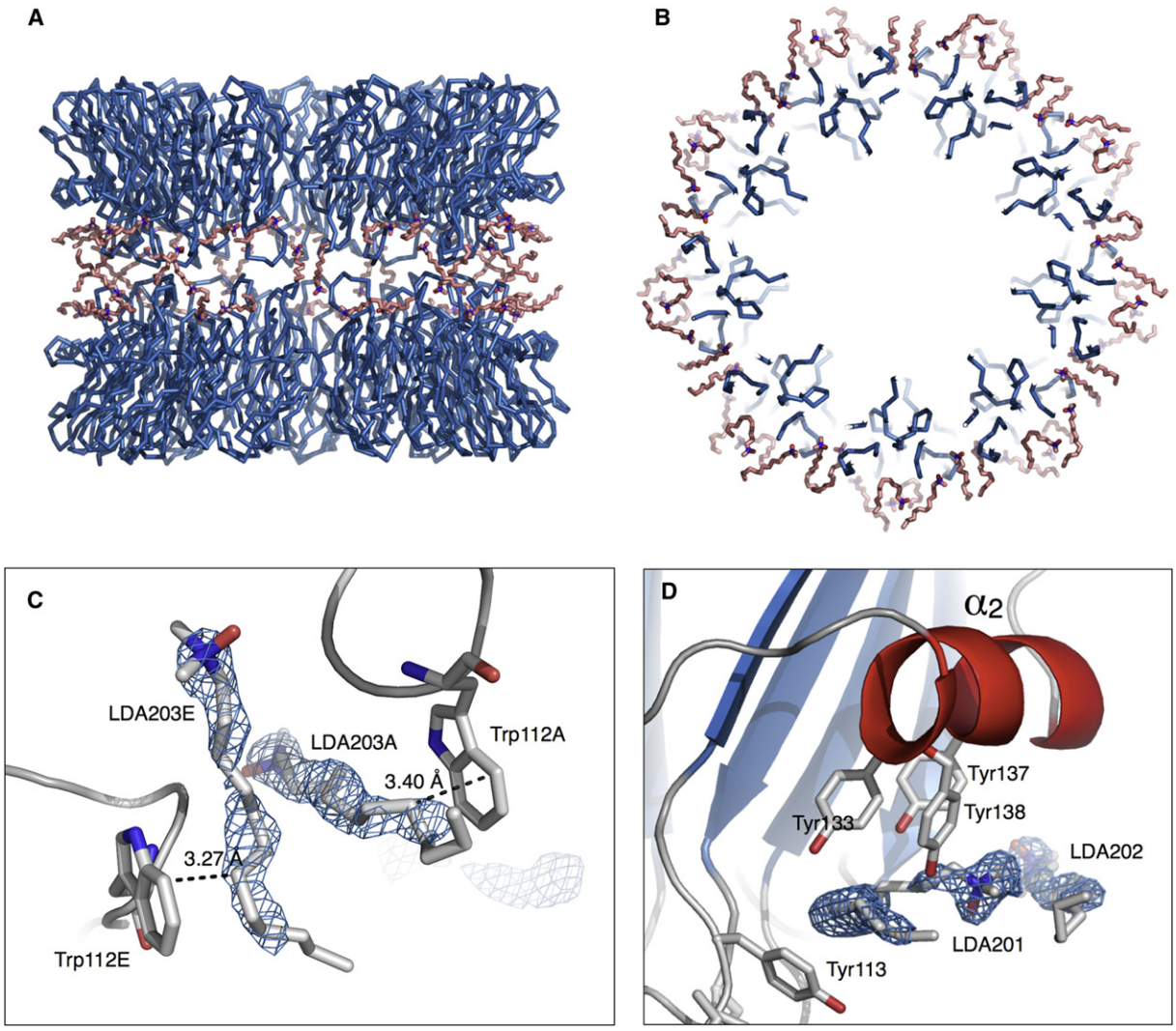

Figure 2. Detergent Molecules in FraC Structure

(A) All LDAO detergent molecules (54 in total, 18 per ASU) were modeled at the interface between two stacking nonamers.

(B) An axial view of a "slice" (of about 3.0 nm thick) of the interface between two FraC rings shows that the detergent distribution is along the periphery of the basal crown rim.

(C) The interactions through the detergent-rich interface do not involve direct protein-protein contacts. This figure shows Trp112 (indicated Trp112A) from the top protomer and the Trp112 (named Trp112E) from the bottom protomer*, that interact through the stacking arrangement of two detergent molecules LDA203 (LDA203A and LDA203E).

(D) The region in which the detergent molecules are located is rich in aromatic residues. Residues Tyr133, Tyr137, and Tyr138 from the α_2 helix orient their aromatic side chain pointing toward the LDAO molecules (LDA201-2). The map in blue around the LDAO molecules corresponds to a $2F_{obs}$-F_{calc} difference map and level 1^{σ}.

*NOTE: both protomers are crystallographically independents.

sequence similarity occurs between members of the actinoporin family (Figure S1). A comparison of the FraC protomer with Eqt-II (Athanasiadis et al., 2001) (RCSB PDB code 1IAZ) and Stn-II (Mancheno et al., 2003) (RCSB PDB code 1GWY) made by superimposing all of the equivalent C_{α} atoms resulted in RMSD values of 0.5 and 0.9 Å, respectively. The superposition of the three β sandwich cores (corresponding to amino acids 32–124, and from 150 to 178 in FraC) showed that the main differences between Eqt-II and Stn-II monomers and the FraC protomer lie in the N-terminal region (Figure 3D; see Supplemental Experimental Procedures). This comparison shows that, in FraC, the N-terminal domain is more "released" from the protein core than in the other two structures. In fact, when the three molecules were analyzed in more detail, we observed that the increase in the solvation free energy (ΔG) between the N termini and their corresponding cores was lower in FraC than in the other two monomeric actinoporin structures (Table S3). These calculations indicated that, if accounting only for the contribution of the solvation energy, the FraC N terminus can detach from the core at a cost about 12% lower than that in Eqt-II or Stn-II.

We observed that Phe16 is located at one end of the α_1 helix of FraC (Figure 3C) and also in Eqt-II (Figure 4A). In monomeric

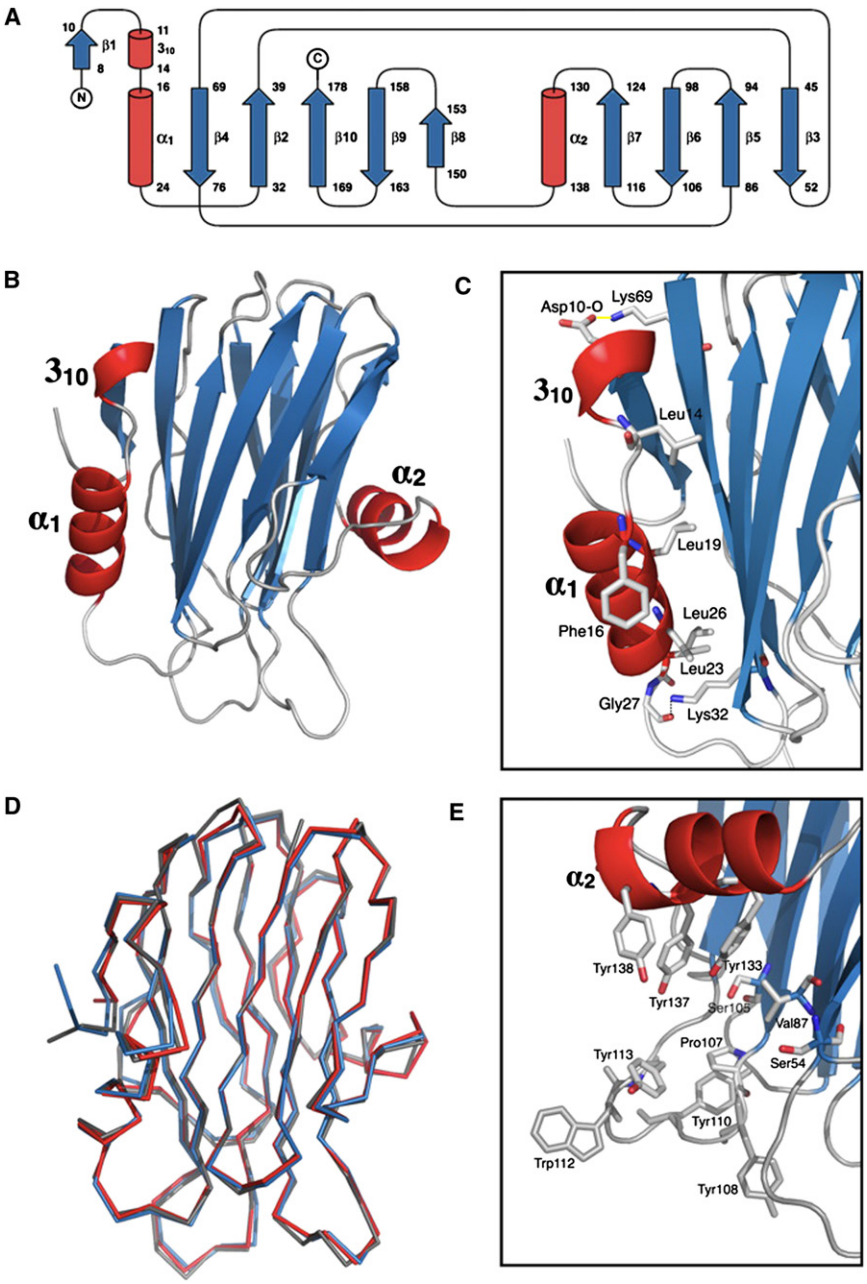

Figure 3. FraC Protomer Structure

(A) The FraC protomer topology is composed of ten β- strands and three short helices (3_{10}, α_1, and α_2).

(B) Ribbon representations of a FraC protomer. The structure consists of a β sandwich core flanked at one side by the β_1-strand, and the 3_{10} and α_1 helices, all located at the N terminus, and at the opposite side by the N-terminal α_2 helix.

(C) The residues that maintain the amphipathic N terminus attached to the β sandwich core are shown as sticks. The interaction established include: a salt bridge between Asp10 and Lys69 (dashed yellow line); hydrophobic interactions between the core and residues Leu14, Leu19, Leu23, and Leu26; and a hydrogen bond between Lys32 and Gly27 (dashed black line).

(D) Superposition of the core α-carbons of the three actinoporin crystal structures: FraC protomer in blue, Eqt-II (RCSB PDB Code 1IAZ) in red, and Stn-II (RCSB PDB Code 1GWY) in gray. Only the α-carbons are shown. The RMSD between α-carbons of FraC and Eqt-II is 0.5 Å, and between FraC and Stn-II is 0.9 Å.

(E) The POC binding site described for Stn-II (Mancheno et al., 2003) is located close to a region rich in aromatic residues. In the case of FraC the POC binding site involve residues Ser54, Val87, Ser105, Pro107, Tyr113, Tyr133, Tyr137, and Tyr138. See also Figure S1.

Eqt-II, the benzyl side chain of Phe16 is pointing to the monomer core, and forming an aromatic cluster with Trp149 and Phe163 (Figure 4A). In oligomeric FraC, however, Ile59 and Val60 (labeled Ile59B and Val60B in Figures 4B, monomer in pink) from the adjacent protomer disrupt these aromatic interactions between Phe16, and the side chains of Trp149 and Phe163 (labeled Phe16A and Trp149A and Phe163A in Figure 4B, monomer in blue).

The short 3_{10} helix observed at the N terminus of the FraC protomer (Figures 3B, 3C, and 4B) is also present in the structures of Eqt-II (RCSB PDB Code 1IAZ) (Figure 4A) and Stn-II (Mancheno et al., 2003) (RCSB PDB code 1GWY). Nevertheless, the authors that solved the structures of these actinoporins did not report this secondary element. This type of helix is also found in the monomeric ClyA (Mueller et al., 2009) (see below).

Cryo-EM Reconstruction of a Functional Pore

An alternative way to induce oligomerization of PFTs in vitro is to incubate the toxin with lipid vesicles (Tilley et al., 2005). Accordingly, to investigate the structure of functional pores, we carried out cryo-EM studies of FraC in the presence of large, unilamellar vesicles (LUV) composed of an equimolar mixture of dioleoyl-phosphatidylcholine (DOPC) and SM. LUVs of this composition were rapidly permeabilized by FraC, and their encapsulated contents were released (Figure S2), indicating the formation of functional pores.

After incubation with FraC, most of the liposomes appeared to be heavily decorated with pores (Figure 5A).

In the cryo-EM micrographs, inserted pores with different orientations could be observed. While in the top (T) and tilted (t) views, the FraC oligomers were observed as small circles, in the side views (S), they appeared as particles with 2-fold symmetry, corresponding to pores lining the edges of the LUVs (top left panel in Figure 5A). A 2D and reference-free image classification of 3,652 manually selected images was used to generate a 3D density map by a common-lines procedure and iterative refinement (see Experimental Procedures). The resulting

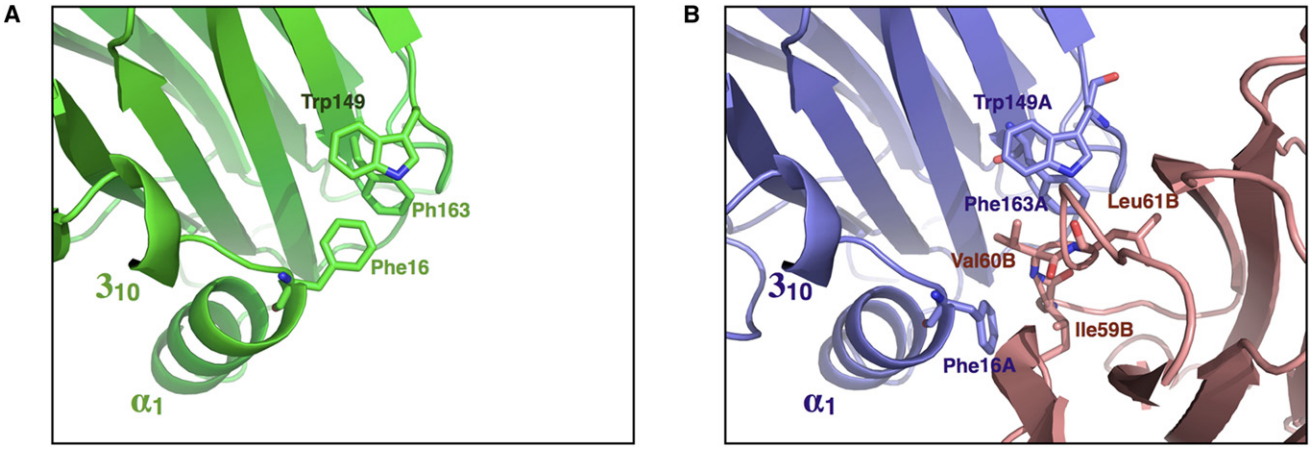

Figure 4. Phe16 Side-Chain Rearrangement upon FraC Oligomerization

(A) In the crystal structure of the monomeric Eqt-II (RCSB PDB Code 1IAZ) the benzyl side chain of Phe16 is fully extended, forming an aromatic cluster with Trp149 and Phe163. The 3_{10} helix at the N-terminal found in FraC is also present in Eqt-II.

(B) In the oligomeric FraC structure, Val60 (indicated as Val60B) from the tenon protomer (model in pink) extends the side chain and interacts with amino acids Trp149 and Phe163 (labeled, respectively, Trp149A and Phe163A) of the mortise protomer (model in blue). Conversely, Phe16 from one mortise protomer strongly interacts with Ile59 at the tenon protomer (see Figure 1F and Table S2B).

map is rendered in Figures 5B (outer surface) and Figure 5C (inner surface). It depicts a landscape in which a well-defined central oligomer (labeled "i") is surrounded by less defined oligomers (labeled "ii"), reflecting the close packing of FraC in these vesicles. A large, extramembrane region lies at the outer surface of the vesicles (Figure 5B), delimiting a conical pore that traverses the membrane, with the narrow opening toward the interior of the vesicle (Figure 5C).

The moderate resolution of the EM map does not allow resolving individual subunits, and the oligomeric state of FraC in the lipid vesicles cannot be observed directly. However, comparisons between the dimensions of the EM map and several possible n-fold oligomers reveal that the overall pore architecture of the cryo-EM reconstruction corresponds nicely with the nonameric structure obtained by X-ray crystallography (Figure S3). Accordingly, we performed a new refinement of the 3D map where 9-fold symmetry was imposed (Figure 5D), yielding improved resolution (~30 Å) (Figure S5) and better defined structural features. In this improved reconstruction a unique central pore emerged to accommodate the crystallographic model of FraC, but the surrounding elements were diffuse due to the averaging imposed by the 9-fold symmetry. The cut-away view in Figure 5E reveals a tapered central pore that resembles a funnel. Its wider internal radius at the top is approximately 5.0 nm, which is similar to that of the crystallographic FraC oligomer (Figure 1C). However, the narrow opening at the bottom is about 1.5 nm in diameter, suggesting that upon membrane binding FraC experiments important conformational changes.

Based on the crystallographic structure and the 9-fold symmetrized cryo-EM map, we built a putative model for a FraC protomer in the membrane-inserted conformation (Figure 6A; see Supplemental Experimental Procedures) and in the corresponding nonameric form (Figure 6B). The model has an extracellular domain made of nine FraC cores, as modeled in the crystal structure, and an α helix tapered bundle spanning the membrane (Figure 5E). The correlation between the cryo-EM map and the nonameric pore improves from 0.78 to 0.8 when inserted α helices are considered (Figures 5D and 5E). Our model has architecture very similar to the transmembrane region observed in the octameric Wza protein, a translocon for *E. coli* capsular polysaccharides (Dong et al., 2006) (Figure 6B, inset). The model for the FraC pore consists of nine contacting helices that contour a pore of 1.5 nm in diameter (Figure 6B).

DISCUSSION

Membrane Binding, Protomer Circularization, and Prepore

The bottom rim of the FraC nonameric structure includes the promoter's basal region which is rich in aromatic residues (Figure 3E). Because tyrosines and tryptophans tend to concentrate at the membrane-water interface (Killian and von Heijne, 2000), we suggest that FraC α_2 helices would lie on the plane of the membrane in the membrane-bound state. These helices would provide anchoring sites to the protomer upon membrane insertion and would contribute to the stability of the β sandwich, which is necessary to build the pore (Kristan et al., 2004).

Oligomerization requires two steps: binding the monomers to the target membrane in the appropriate orientation ("up and down" or "vertical" orientation), and bringing the monomers (protomers) into contact through the oligomerization interface ('lateral' orientation). In the case of Eqt-II, an exposed aromatic-rich loop (residues 106–116) has been shown to participate in initial binding to the target membrane (Hong et al., 2002; Kristan et al., 2004). Consequently, this exposed aromatic-rich loop facilitates oligomerization by helping to discriminate between up and down (Hong et al., 2002; Malovrh et al., 2003). Lateral orientation is achieved by the POC binding site and its specific affinity for the interfaces of coexisting lipid phases (Alegre-Cebollada et al., 2006; Barlic et al., 2004). Thus, toxin monomers might form a one-dimensional array along the lipid

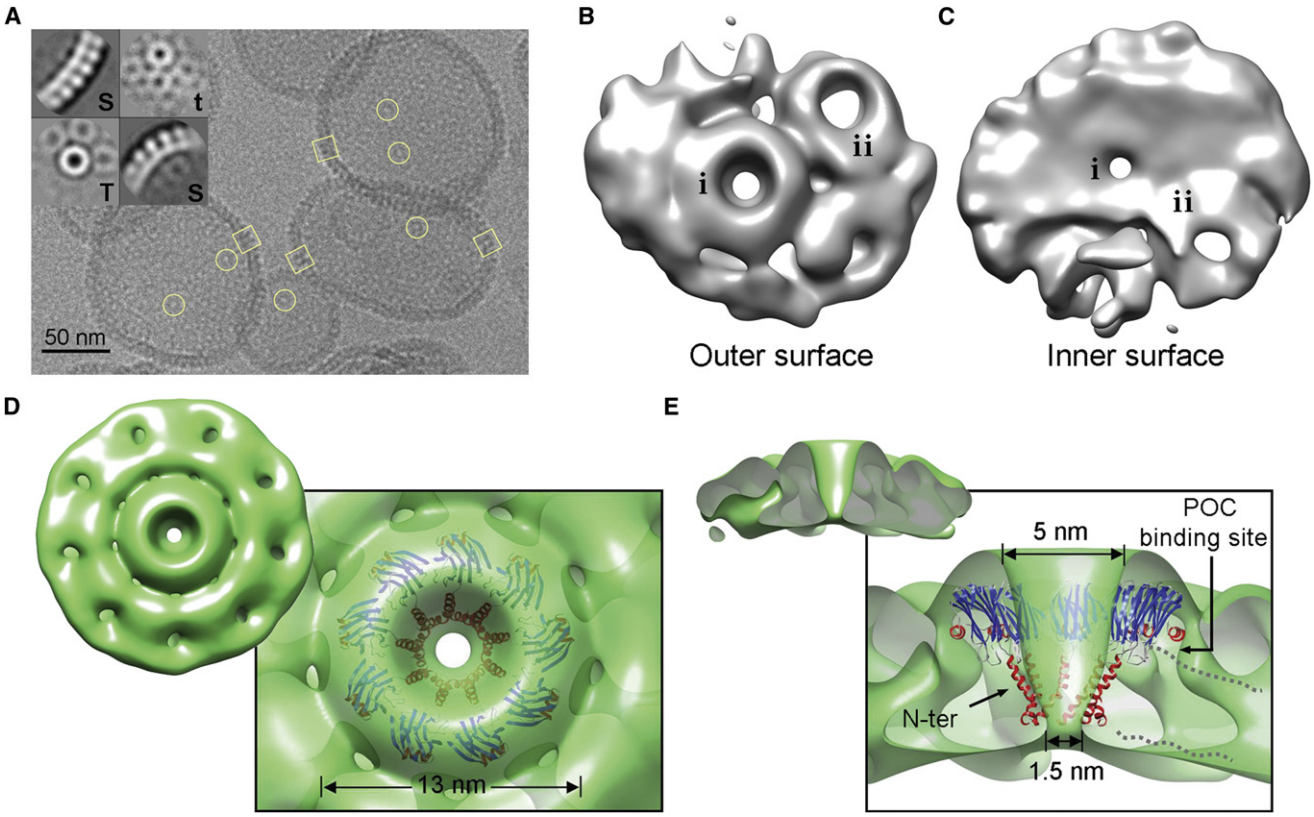

Figure 5. Cryo-EM of FraC Pores in Lipid Vesicles

(A) Field of a cryo-EM micrograph showing FraC pores inserted in LUVs. Representative views are enclosed within circles (top and tilted views) or squares (side views). The inset shows some of the averages obtained after 2D classification. These averages are attributed to top (T), side (S), or tilted (t) views of the oligomeric pores. Rendering the cryo-EM map for FraC pores without imposed symmetry shown as seen from the outer (B) or inner (C) surface of the vesicles. The top (D) and cut-away side (E) semitransparent renderings of the 9-fold symmetry 3D map allow for visualization of the fitted atomic model for FraC with the N-terminal amphipathic α helices inserted into the membrane. The dashed gray lines in (E) delineate the approximate width of the lipid bilayer. The thumbnails in (D) and (E) indicate the orientations of the panels. See also Figures S2–S5.

interfaces with their α_2 helices facing the SM-rich phase. This orientation leaves the protein face containing the mortise and that containing the tenon pointing toward opposite directions along the lipid interface. Most likely, these events help oligomerization because they brings into contact the complementary sides of the protomers that eventually form the pore. Accumulation of the toxin along this one-dimensional space not only acts as an efficient concentration strategy but also releases the linear tension that keeps the lipid phases apart and results in lipid mixing (Garcia-Saez et al., 2007). In random binding, the assembly of functional nonamers within the plane of the membrane would be a very unlikely event, and high concentrations of the toxin would be needed to observe lytic effects. In contrast, actinoporins exhibit their lytic effects even at subnanomolar concentrations (Macek and Lebez, 1988). However, although hemolysis occurs quickly, it does not take place immediately after the addition of the toxin to an erythrocyte suspension. Instead, a concentration-dependent lag precedes hemolysis (Macek and Lebez, 1981), which probably corresponds to the time needed for the toxin monomers to reach the cell and oligomerize to make a prepore, the structure preceding the functional pore. This delay has been observed for Eqt-II in giant unilamellar vesicles (GUV), in which, after a lag time of approximately 20 min, the vesicles are permeabilized within 1 to 5 min (Schon et al., 2008).

As mentioned before, in the FraC oligomer, α_1 helices face the internal crown surface and attach to the main β sandwiches. Because the N termini must be inserted into the membrane for functional pore formation, the crystal structure of FraC represents a nonlytic conformation. This oligomeric structure is fully compatible with our cryo-EM reconstruction of functional pores. Therefore, the crystallographic FraC oligomer (Figures 1C and 1D) can be assumed to be a high-resolution model of an actinoporin in its prepore state.

Prepore to Pore Transition

Once an actinoporin is attached to the target cell, the N-terminal α helix must reorient and penetrate the membrane to make a membrane pore (Gutierrez-Aguirre et al., 2004; Hong et al., 2002; Malovrh et al., 2003). This change in conformation at the N terminus appears to be coupled to oligomerization (Macek et al., 1995), but the molecular events triggering release of the α_1 helix from the protein core are not completely understood. The FraC crystal structure allows us to better understand how

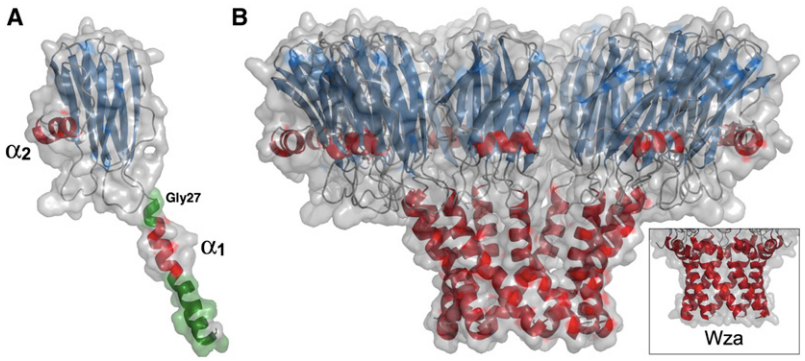

Figure 6. FraC Pore Model

(A) The X-ray crystallographic FraC protomer structure was used to build a model in the membrane inserted conformation (see Supplemental Experimental Procedures). The N-terminal undergoes the major rearrangement including detachment from the protein core, a rotation of about 180°, and the extension of its helical segment (compare this model with Figure 3B). Amino acids 2–27 were rotated as a rigid body around Gly27, and the two nonhelical portions (residues 2–15 and 25–27, shown in green) were forced to adopt a continuous α helix structure.

(B) The application of 9-fold symmetry to the protomer structure yields a putative model of the functional pore. Inset: α-helical bundle corresponding to the transmembrane region of Wza, a translocon for *E. coli* capsular polysaccharides (Dong et al., 2006) (RCSB PDB Code 2J58).

the oligomerization process can drive the necessary structural changes that promote membrane permeation.

It has already been established that membrane insertion may proceed through the M2 intermediary (Alegre-Cebollada et al., 2007), in which the α_1 helix detaches from the main body of the molecule and resides transiently at the membrane-water interface (Hong et al., 2002; Malovrh et al., 2003). The α_1 helix in FraC runs from Phe16 to Glu24, in Eqt-II, it includes residues Phe16 to Leu26, and in Stn-II, this helix consists of Thr13 to Glu23. However, when inserted into the membrane, the N-terminal α helix of Eqt-II extends from Asp10 to Asp28 (Malovrh et al., 2003). This elongation is necessary to cross the lipid bilayer, which spans a distance of about 3–4 nm. Regarding the limited space in the FraC structure, the α_1 helix must elongate after the N terminus has changed its orientation, contacting the lipids in the central lumen.

One interesting feature of actinoporins is the presence of a one-turn 3_{10} helix located at the N terminus between the β_2 strands and the α_1 helix. The α helix is the predominant type of helix found in protein structure, with an occurrence of about 80%. Only 20% of these helices correspond to 3_{10} helices (Barlow and Thornton, 1988). Interestingly, 3_{10} helices have been proposed to be intermediates in the folding/unfolding of α helices (Millhauser, 1995). Moreover, molecular dynamic simulations in polypeptides have indicated that the propensity of α-helical conformations increases with the hydrophobicity of the medium, whereas for 3_{10} helices, the propensity decreases (Sorin et al., 2006). This characteristic of 3_{10} helices is consistent with the fact that the N-terminal segment in actinoporins converts into a long α helix upon membrane insertion.

The conversion of a 3_{10} helix into an α helix following membrane binding has been observed in ClyA. The ClyA monomer consists of a long four helix bundle with a subdomain named the β-tongue, and this subdomain contains two short 3_{10} helices, one at the N terminus of helix D and a second in the loop connecting strands β_1 and β_2 (Wallace et al., 2000). This region undergoes a structural rearrangement to change into a long α helix in the membrane-bound state (Mueller et al., 2009). Analogous to what has been observed in ClyA, we propose that, in actinoporins, the transition from the nonlytic conformation to a functional pore includes a hypothetical intermediate state that resembles the conformational switch observed in the extension of helices in ClyA (Mueller et al., 2009).

Upon membrane insertion, the N-terminal segment is transferred across the bilayer (Kristan et al., 2007). In FraC, this transition is most likely mediated by Gly27, which is located in a loop at the base of the protomer and is hydrogen-bonded to Lys32. This residue might function as a hinge that facilitates this significant conformational change. In fact, in Eqt-II, a Gly27Cys mutation decreases its hemolytic activity to 17% of that of wild-type (Malovrh et al., 2003). A fact that supports that Gly27 and Lys32 play an important role is that these two residues are conserved in all actinoporins described so far (Figure S1).

We propose that, upon oligomerization, Val60 from one protomer (tenon) displaces Phe16 from the adjacent protomer (mortise), disrupting the interactions within the aromatic cluster Phe16-Phe163-Trp149. The side chain of Phe16 (Phe16A, in Figure 4B) changes its orientation that was occupying in the monomeric state (most likely identical to Phe16 of Eqt-II, as is shown in Figure 4A), and, in this new conformation, interacts with the Ile59 from the neighboring protomer (Ile59B in Figure 4B). This switching of the Phe16 interaction may cause the release of the N-terminal from the β sandwich, allowing it to detach from the core and reach the membrane surface. Once in contact with the lipids, the hydrophobic environment triggers elongation of the α helix and insertion into the membrane. Hence, in our mechanistic view, prepore formation is a crucial step because it may also allow membrane insertion. However, oligomerization is necessary, but not sufficient, to induce the N-terminal conformational change. The presence of a bilayer with an appropriate lipid composition is also required for PFTs to permeate membranes.

Hypothetical α-Helical Bundle Pore Model

In solution, FraC permeabilizes LUVs made of a model lipid composition DOPC:SM (1:1) (Bellomio et al., 2009). Cryo-EM images of these model membranes incubated with FraC show that the toxin makes ring-like structures that cover the entire membrane surface. The 3D reconstruction of the ring-like motif reveals a conical shape that traverses the membrane with the smaller aperture toward the inner space of the vesicle. Improving the reconstruction by averaging with 9-fold symmetry, we find a map shaping a funnel with large and small apertures of about 5.0 and 1.5 nm, respectively (Figures 5D and 5E). As the estimated functional pore diameter of other actinoporins is about

2 nm (Alvarez et al., 2009; Belmonte et al., 1993; de los Rios et al., 1998; Tejuca et al., 2001), our cryo-EM reconstruction of the FraC pore is in full agreement with former biochemical studies.

In turn, the cryo-EM reconstruction of functional FraC pores supports the physiological relevance of the nonameric crystallographic model. Consequently, we constructed a pore model in which the nine N termini assemble as a compact α-helical bundle. In contrast to proposals for the toroidal model (Alvarez et al., 2009; Kristan et al., 2009; Mancheno et al., 2003), in our actinoporin pore model, lipids are not part of the pore wall.

In conclusion, the work presented here includes a high-resolution crystal structure and cryo-EM reconstructions of FraC inserted into a membrane, shedding light on the architecture and sequential events that lead to pore formation by actinoporins. Furthermore, our FraC pore model agrees with a concept that emerged from examining the structure oligomeric ClyA: a membrane pore can be constructed exclusively with protein arranged in an α-helical bundle.

EXPERIMENTAL PROCEDURES

FraC Purification, Crystallization, and Structure Resolution

Full details of FraC purification (Bellomio et al., 2009), crystallization and data collection have been recently published (Mechaly et al., 2009). FraC structure was solved by molecular replacement (MR) with the program Phaser (McCoy, 2007) and using as searching model one monomer of Eqt-II structure (Athanasiadis et al., 2001; RCSB PDB Code: 1IAZ). The MR solution was found in space group $P6_322$ and contained six molecules per asymmetric unit. After the first round of structure and anisotropic B factor refinement with the program phenix.refine (Adams et al., 2004), many clear elongated regions of positive electron density were observed. These regions were located close to the aromatic rings of Trp112 and into a site corresponding to the POC binding site described in Stn-II (Mancheno et al., 2003). At this stage the MR solution was modified with the program Coot (Emsley and Cowtan, 2004) to change the amino acids to those corresponding to the FraC sequence. Further refinement rounds included noncrystallographic symmetry (NCS) restrictions and model rebuilding by addition of both water and LDAO molecules. The LDAO detergent molecules were traced within the elongated regions of the $2F_{obs}$- F_{calc} and F_{obs}-F_{calc} maps. Within the asymmetric unit, a total of 938 water and 18 LDAO molecules were modeled (Table S1). The final FraC model has a good quality as estimated by the program MolProbity (Davis et al., 2007) and corresponds to a 1.8 Å resolution structure. The overall R_{cryst} and R_{free} values are 19% and 23%, respectively (Table S1).

Lipid Vesicles Preparation

The encapsulation of ANTS and DPX in LUVs of DOPC-SM (1:1) and FraC-mediated permeabilization of the vesicles were carried out as previously described (Bellomio et al., 2009). LUVs of the same lipid composition used for cryo-EM were prepared by extrusion (Mayer et al., 1986). The lipids dissolved in chloroform:methanol (2:1) were dried with N_2 in a glass tube and then placed 2 hr in vacuum to remove traces of chloroform. They were then resuspended in 10 mM HEPES, 50 mM NaCl (pH 7.5) and subjected to ten cycles of freezing and thawing in liquid nitrogen and a 45°C water bath. The lipid suspension was extruded 10 times through polycarbonate filters with a pore diameter of 0.1 μm (Nucleopore, Pleasanton, CA) to obtain LUVs 1 mM lipids final concentration.

Cryo-EM of FraC Inserted in Model Membranes

For cryo-EM studies, LUVs were incubated with FraC (1 mg/ml) for 30 min. Cryo-EM grids were prepared following standard procedures and observed at liquid nitrogen temperature in a JEM-2200FS/CR transmission electron microscope (JEOL Europe, Croissy-sur-Seine, France) operated at 200 kV. An in-column omega energy filter helped to record images with improved signal to noise ratio by zero-loss filtering. Digital images were recorded on CCD camera under low-dose conditions, at a magnification of 86,862 obtaining a final pixel size of 1.72 Å/pixel. Manual selection provided a set of 3652 individual particles for pores in LUV of DOPC-SM.

The images were CTF-corrected by flipping phases after estimation of CTF parameters in EMAN (Ludtke et al., 1999). The 2D images were classified by maximum-likelihood-based procedures within the XMIPP (Scheres et al., 2008). The starting 3D model was generated using reference-free alignment, classification and common-lines procedures implemented in EMAN. This was followed by iterative refinement using a projection matching scheme in SPIDER package (Baxter et al., 2007).

The rigid body fitting was performed semiautomatically by maximization of the sum of map values at atom positions, and by improvement in the coefficient of correlation between simulated maps from the atomic structures and the cryo-EM density map in Chimera (Pettersen et al., 2004). This software was also used to create the figures. The cryo-EM maps were calculated with no symmetry or imposing 9-fold symmetry. The total set of images was split into two halves, two density maps were calculated and the resolution was estimated by Fourier Shell Correlation at 0.5 and 0.15 thresholds between these two maps. Additionally, correlations between the atomic structure of FraC and the 9-fold symmetrized cryo-EM map suggest a resolution around 30 Å (Figure S5).

ACCESSION NUMBERS

Atomic coordinates and structure factors for the oligomeric FraC have been deposited in the RCSB PDB under the accession number 3LIM.

SUPPLEMENTAL INFORMATION

Supplemental Information includes Supplemental Experimental Procedures, five figures, and three tables and can be found with this article online at doi:10.1016/j.str.2010.11.013.

ACKNOWLEDGMENTS

We thank Prof. Felix Goñi and Prof. Mario Amzel for helpful discussions and for critical reading of the manuscript. This work was partially supported by the MICINN, the Basque Government (Etortek Research Program 2008/2010), Bizkaia::Xede and Bizkaia County, Spain. A.E.M. was a recipient of a fellowship from the MICINN, Spain. K.M. is a recipient of a fellowship from the MICINN, Spain. A.B. is a staff scientist from the CONICET (Argentina) and received a visiting scientist fellowship from the Basque Government while conducting this work. We acknowledge the use of the ESRF beamline ID14-4.

Received: July 5, 2010
Revised: November 1, 2010
Accepted: November 6, 2010
Published: February 8, 2011

REFERENCES

Abrami, L., Kunz, B., Iacovache, I., and van der Goot, F.G. (2008). Palmitoylation and ubiquitination regulate exit of the Wnt signaling protein LRP6 from the endoplasmic reticulum. Proc. Natl. Acad. Sci. USA *105*, 5384–5389.

Adams, P.D., Gopal, K., Grosse-Kunstleve, R.W., Hung, L.W., Ioerger, T.R., McCoy, A.J., Moriarty, N.W., Pai, R.K., Read, R.J., Romo, T.D., et al. (2004). Recent developments in the PHENIX software for automated crystallographic structure determination. J. Synchrotron Radiat. *11*, 53–55.

Alegre-Cebollada, J., Rodriguez-Crespo, I., Gavilanes, J.G., and del Pozo, A.M. (2006). Detergent-resistant membranes are platforms for actinoporin pore-forming activity on intact cells. FEBS J. *273*, 863–871.

Alegre-Cebollada, J., Onaderra, M., Gavilanes, J.G., and del Pozo, A.M. (2007). Sea anemone actinoporins: the transition from a folded soluble state to a functionally active membrane-bound oligomeric pore. Curr. Protein Pept. Sci. *8*, 558–572.

Allende, D., Simon, S.A., and McIntosh, T.J. (2005). Melittin-induced bilayer leakage depends on lipid material properties: evidence for toroidal pores. Biophys. J. *88*, 1828–1837.

Alvarez, C., Mancheno, J.M., Martinez, D., Tejuca, M., Pazos, F., and Lanio, M.E. (2009). Sticholysins, two pore-forming toxins produced by the Caribbean Sea anemone Stichodactyla helianthus: their interaction with membranes, *54* (Toxicon), 1135–1147.

Anderluh, G., and Lakey, J.H. (2008). Disparate proteins use similar architectures to damage membranes. Trends Biochem. Sci. *33*, 482–490.

Astier, Y., Bayley, H., and Howorka, S. (2005). Protein components for nanodevices. Curr. Opin. Chem. Biol. *9*, 576–584.

Athanasiadis, A., Anderluh, G., Macek, P., and Turk, D. (2001). Crystal structure of the soluble form of equinatoxin II, a pore-forming toxin from the sea anemone Actinia equina. Structure *9*, 341–346.

Bakrac, B., Gutierrez-Aguirre, I., Podlesek, Z., Sonnen, A.F., Gilbert, R.J., Macek, P., Lakey, J.H., and Anderluh, G. (2008). Molecular determinants of sphingomyelin specificity of a eukaryotic pore-forming toxin. J. Biol. Chem. *283*, 18665–18677.

Barlic, A., Gutierrez-Aguirre, I., Caaveiro, J.M., Cruz, A., Ruiz-Arguello, M.B., Perez-Gil, J., and Gonzalez-Manas, J.M. (2004). Lipid phase coexistence favors membrane insertion of equinatoxin-II, a pore-forming toxin from Actinia equina. J. Biol. Chem. *279*, 34209–34216.

Barlow, D.J., and Thornton, J.M. (1988). Helix geometry in proteins. J. Mol. Biol. *201*, 601–619.

Baxter, W.T., Leith, A., and Frank, J. (2007). SPIRE: the SPIDER reconstruction engine. J. Struct. Biol. *157*, 56–63.

Bayley, H. (2009). Membrane-protein structure: Piercing insights. Nature *459*, 651–652.

Bellomio, A., Morante, K., Barlic, A., Gutierrez-Aguirre, I., Viguera, A.R., and Gonzalez-Manas, J.M. (2009). Purification, cloning and characterization of fragaceatoxin C, a novel actinoporin from the sea anemone Actinia fragacea. Toxicon *54*, 869–880.

Belmonte, G., Pederzolli, C., Macek, P., and Menestrina, G. (1993). Pore formation by the sea anemone cytolysin equinatoxin II in red blood cells and model lipid membranes. J. Membr. Biol. *131*, 11–22.

Bischofberger, M., Gonzalez, M.R., and van der Goot, F.G. (2009). Membrane injury by pore-forming proteins. Curr. Opin. Cell. Biol. *21*, 589–595.

Dang, T.X., Hotze, E.M., Rouiller, I., Tweten, R.K., and Wilson-Kubalek, E.M. (2005). Prepore to pore transition of a cholesterol-dependent cytolysin visualized by electron microscopy. J. Struct. Biol. *150*, 100–108.

Davis, I.W., Leaver-Fay, A., Chen, V.B., Block, J.N., Kapral, G.J., Wang, X., Murray, L.W., Arendall, W.B., 3rd, Snoeyink, J., Richardson, J.S., and Richardson, D.C. (2007). MolProbity: all-atom contacts and structure validation for proteins and nucleic acids. Nucleic Acids Res. *35*, W375–W383.

de los Rios, V., Mancheno, J.M., Lanio, M.E., Onaderra, M., and Gavilanes, J.G. (1998). Mechanism of the leakage induced on lipid model membranes by the hemolytic protein sticholysin II from the sea anemone Stichodactyla helianthus. Eur. J. Biochem. *252*, 284–289.

Dong, C., Beis, K., Nesper, J., Brunkan-Lamontagne, A.L., Clarke, B.R., Whitfield, C., and Naismith, J.H. (2006). Wza the translocon for E. coli capsular polysaccharides defines a new class of membrane protein. Nature *444*, 226–229.

Eifler, N., Vetsch, M., Gregorini, M., Ringler, P., Chami, M., Philippsen, A., Fritz, A., Muller, S.A., Glockshuber, R., Engel, A., and Grauschopf, U. (2006). Cytotoxin ClyA from Escherichia coli assembles to a 13-meric pore independent of its redox-state. EMBO J. *25*, 2652–2661.

Emsley, P., and Cowtan, K. (2004). Coot: model-building tools for molecular graphics. Acta Crystallogr. D Biol. Crystallogr. *60*, 2126–2132.

Garcia, K.C., Degano, M., Pease, L.R., Huang, M., Peterson, P.A., Teyton, L., and Wilson, I.A. (1998). Structural basis of plasticity in T cell receptor recognition of a self peptide-MHC antigen. Science *279*, 1166–1172.

Garcia-Saez, A.J., Chiantia, S., and Schwille, P. (2007). Effect of line tension on the lateral organization of lipid membranes. J. Biol. Chem. *282*, 33537–33544.

Gonzalez, M.R., Bischofberger, M., Pernot, L., van der Goot, F.G., and Freche, B. (2008). Bacterial pore-forming toxins: the (w)hole story? Cell Mol. Life Sci. *65*, 493–507.

Gouaux, E. (1997). Channel-forming toxins: tales of transformation. Curr. Opin. Struct. Biol. *7*, 566–573.

Gutierrez-Aguirre, I., Barlic, A., Podlesek, Z., Macek, P., Anderluh, G., and Gonzalez-Manas, J.M. (2004). Membrane insertion of the N-terminal alpha-helix of equinatoxin II, a sea anemone cytolytic toxin. Biochem. J. *384*, 421–428.

Hong, Q., Gutierrez-Aguirre, I., Barlic, A., Malovrh, P., Kristan, K., Podlesek, Z., Macek, P., Turk, D., Gonzalez-Manas, J.M., Lakey, J.H., and Anderluh, G. (2002). Two-step membrane binding by Equinatoxin II, a pore-forming toxin from the sea anemone, involves an exposed aromatic cluster and a flexible helix. J. Biol. Chem. *277*, 41916–41924.

Killian, J.A., and von Heijne, G. (2000). How proteins adapt to a membrane-water interface. Trends Biochem. Sci. *25*, 429–434.

Kristan, K., Podlesek, Z., Hojnik, V., Gutierrez-Aguirre, I., Guncar, G., Turk, D., Gonzalez-Manas, J.M., Lakey, J.H., Macek, P., and Anderluh, G. (2004). Pore formation by equinatoxin, a eukaryotic pore-forming toxin, requires a flexible N-terminal region and a stable beta-sandwich. J. Biol. Chem. *279*, 46509–46517.

Kristan, K., Viero, G., Macek, P., Dalla Serra, M., and Anderluh, G. (2007). The equinatoxin N-terminus is transferred across planar lipid membranes and helps to stabilize the transmembrane pore. FEBS J. *274*, 539–550.

Kristan, K.C., Viero, G., Dalla Serra, M., Macek, P., and Anderluh, G. (2009). Molecular mechanism of pore formation by actinoporins. Toxicon *54*, 1125–1134.

Kroemer, G., Galluzzi, L., and Brenner, C. (2007). Mitochondrial membrane permeabilization in cell death. Physiol. Rev. *87*, 99–163.

Iacovache, I., van der Goot, F.G., and Pernot, L. (2008). Pore formation: an ancient yet complex form of attack. Biochim. Biophys. Acta. *1778*, 1611–1623.

Iacovache, I., Bischofberger, M., and van der Goot, F.G. (2010). Structure and assembly of pore-forming proteins. Curr. Opin. Struct. Biol. *20*, 241–246.

Lashuel, H.A., and Lansbury, P.T., Jr. (2006). Are amyloid diseases caused by protein aggregates that mimic bacterial pore-forming toxins? Q. Rev. Biophys. *39*, 167–201.

Lawrence, M.C., and Colman, P.M. (1993). Shape complementarity at protein/protein interfaces. J. Mol. Biol. *234*, 946–950.

Ludtke, S.J., Baldwin, P.R., and Chiu, W. (1999). EMAN: semiautomated software for high-resolution single-particle reconstructions. J. Struct. Biol. *128*, 82–97.

Macek, P., and Lebez, D. (1981). Kinetics of hemolysis induced by equinatoxin, a cytolytic toxin from the sea anemone Actinia equina. Effect of some ions and pH. Toxicon *19*, 233–240.

Macek, P., and Lebez, D. (1988). Isolation and characterization of three lethal and hemolytic toxins from the sea anemone Actinia equina L. Toxicon *26*, 441–451.

Macek, P., Zecchini, M., Pederzolli, C., Dalla Serra, M., and Menestrina, G. (1995). Intrinsic tryptophan fluorescence of equinatoxin II, a pore-forming polypeptide from the sea anemone Actinia equina L, monitors its interaction with lipid membranes. Eur. J. Biochem. *234*, 329–335.

Malovrh, P., Viero, G., Serra, M.D., Podlesek, Z., Lakey, J.H., Macek, P., Menestrina, G., and Anderluh, G. (2003). A novel mechanism of pore formation: membrane penetration by the N-terminal amphipathic region of equinatoxin. J. Biol. Chem. *278*, 22678–22685.

Mancheno, J.M., Martin-Benito, J., Martinez-Ripoll, M., Gavilanes, J.G., and Hermoso, J.A. (2003). Crystal and electron microscopy structures of sticholysin II actinoporin reveal insights into the mechanism of membrane pore formation. Structure *11*, 1319–1328.

Mancheño, J.M., Martin-Benito, J., Gavilanes, J.G., and Vazquez, L. (2006). A complementary microscopy analysis of Sticholysin II crystals on lipid films: Atomic force and transmission electron characterizations. Biophys. Chem. *119*, 219–223.

Martin-Benito, J., Gavilanes, F., de Los Rios, V., Mancheno, J.M., Fernandez, J.J., and Gavilanes, J.G. (2000). Two-dimensional crystallization on lipid monolayers and three-dimensional structure of sticholysin II, a cytolysin from the sea anemone Stichodactyla helianthus. Biophys. J. *78*, 3186–3194.

Mayer, L.D., Hope, M.J., and Cullis, P.R. (1986). Vesicles of variable sizes produced by a rapid extrusion procedure. Biochim. Biophys. Acta *858*, 161–168.

McCoy, A.J. (2007). Solving structures of protein complexes by molecular replacement with Phaser. Acta Crystallogr. D Biol. Crystallogr. *63*, 32–41.

Mechaly, A.E., Bellomio, A., Morante, K., Gonzalez-Manas, J.M., and Guerin, D.M. (2009). Crystallization and preliminary crystallographic analysis of fragaceatoxin C, a pore-forming toxin from the sea anemone Actinia fragacea. Acta Crystallogr. Sect. F Struct. Biol. Cryst. Commun. *65*, 357–360.

Millhauser, G.L. (1995). Views of helical peptides: a proposal for the position of 3(10)-helix along the thermodynamic folding pathway. Biochemistry *34*, 3873–3877.

Mueller, M., Grauschopf, U., Maier, T., Glockshuber, R., and Ban, N. (2009). The structure of a cytolytic α-helical toxin pore reveals its assembly mechanism. Nature *459*, 726–730.

Olson, R., Nariya, H., Yokota, K., Kamio, Y., and Gouaux, E. (1999). Crystal structure of staphylococcal LukF delineates conformational changes accompanying formation of a transmembrane channel. Nat. Struct. Biol. *6*, 134–140.

Panchal, R.G., Smart, M.L., Bowser, D.N., Williams, D.A., and Petrou, S. (2002). Pore-forming proteins and their application in biotechnology. Curr. Pharm. Biotechnol. *3*, 99–115.

Parker, M.W., and Feil, S.C. (2005). Pore-forming protein toxins: from structure to function. Prog. Biophys. Mol. Biol. *88*, 91–142.

Pettersen, E.F., Goddard, T.D., Huang, C.C., Couch, G.S., Greenblatt, D.M., Meng, E.C., and Ferrin, T.E. (2004). UCSF Chimera—a visualization system for exploratory research and analysis. J. Comput. Chem. *25*, 1605–1612.

Potrich, C., Tomazzolli, R., Dalla Serra, M., Anderluh, G., Malovrh, P., Macek, P., Menestrina, G., and Tejuca, M. (2005). Cytotoxic activity of a tumor protease-activated pore-forming toxin. Bioconjug. Chem. *16*, 369–376.

Rossjohn, J., Feil, S.C., McKinstry, W.J., Tweten, R.K., and Parker, M.W. (1997). Structure of a cholesterol-binding, thiol-activated cytolysin and a model of its membrane form. Cell *89*, 685–692.

Scheres, S.H., Nunez-Ramirez, R., Sorzano, C.O., Carazo, J.M., and Marabini, R. (2008). Image processing for electron microscopy single-particle analysis using XMIPP. Nat. Protoc. *3*, 977–990.

Schon, P., Garcia-Saez, A.J., Malovrh, P., Bacia, K., Anderluh, G., and Schwille, P. (2008). Equinatoxin II permeabilizing activity depends on the presence of sphingomyelin and lipid phase coexistence. Biophys. J. *95*, 691–698.

Sobko, A.A., Kotova, E.A., Antonenko, Y.N., Zakharov, S.D., and Cramer, W.A. (2004). Effect of lipids with different spontaneous curvature on the channel activity of colicin E1: evidence in favor of a toroidal pore. FEBS Lett. *576*, 205–210.

Song, L., Hobaugh, M.R., Shustak, C., Cheley, S., Bayley, H., and Gouaux, J.E. (1996). Structure of staphylococcal alpha-hemolysin, a heptameric transmembrane pore. Science *274*, 1859–1866.

Sorin, E.J., Rhee, Y.M., Shirts, M.R., and Pande, V.S. (2006). The solvation interface is a determining factor in peptide conformational preferences. J. Mol. Biol. *356*, 248–256.

Tejuca, M., Serra, M.D., Ferreras, M., Lanio, M.E., and Menestrina, G. (1996). Mechanism of membrane permeabilization by sticholysin I, a cytolysin isolated from the venom of the sea anemone Stichodactyla helianthus. Biochemistry *35*, 14947–14957.

Tejuca, M., Dalla Serra, M., Potrich, C., Alvarez, C., and Menestrina, G. (2001). Sizing the radius of the pore formed in erythrocytes and lipid vesicles by the toxin sticholysin I from the sea anemone Stichodactyla helianthus. J. Membr. Biol. *183*, 125–135.

Tilley, S.J., Orlova, E.V., Gilbert, R.J., Andrew, P.W., and Saibil, H.R. (2005). Structural basis of pore formation by the bacterial toxin pneumolysin. Cell *121*, 247–256.

Tweten, R.K. (2005). Cholesterol-dependent cytolysins, a family of versatile pore-forming toxins. Infect. Immun. *73*, 6199–6209.

Walker, B., Krishnasastry, M., Zorn, L., and Bayley, H. (1992). Assembly of the oligomeric membrane pore formed by Staphylococcal alpha-hemolysin examined by truncation mutagenesis. J. Biol. Chem. *267*, 21782–21786.

Walker, B., Braha, O., Cheley, S., and Bayley, H. (1995). An intermediate in the assembly of a pore-forming protein trapped with a genetically-engineered switch. Chem. Biol. *2*, 99–105.

Wallace, A.J., Stillman, T.J., Atkins, A., Jamieson, S.J., Bullough, P.A., Green, J., and Artymiuk, P.J. (2000). E. coli hemolysin E (HlyE, ClyA, SheA): X-ray crystal structure of the toxin and observation of membrane pores by electron microscopy. Cell *100*, 265–276.

Yang, L., Harroun, T.A., Weiss, T.M., Ding, L., and Huang, H.W. (2001). Barrel-stave model or toroidal model? A case study on melittin pores. Biophys. J. *81*, 1475–1485.